Direct Wind-Powered Desalination System

David Keisar,[*] Viatcheslav Freger[†] and David Greenblatt[*]

[*]*Faculty of Mechanical Engineering, Technion – Israel Institute of Technology*

[†]*Faculty of Chemical Engineering, Technion – Israel Institute of Technology*

Abstract

A novel direct wind-powered desalination (D-WPD) system for brackish water utilizes a small-scale vertical axis wind turbine to directly power a reverse-osmosis-based desalination system via a high-pressure pump without electricity generation or a system controller. A comprehensive parametric study examined the effects of feed water salinity, module loading, and wind speed on the system's performance, demonstrating high efficiency under various operating conditions. A stand-alone system demonstrated operation at effectively constant system efficiency, approximately 13.5%, and low specific wind and mechanical energy consumptions for a wide range of wind speeds and salinities. Despite the turbine's small projected area of 0.8m^2, the D-WPD system yielded a daily permeate production of up to 0.6 m^3/day at an average wind speed of 6 m/s. The D-WPD system surpassed previous wind-powered desalination studies in terms of specific energy consumption, relative efficiency, and relative desalination capacity, making it a low-cost solution for off-grid wind-powered small-scale desalination. Combined with the system's low noise emission and reduced probability of bird strikes, a desalination system based on these findings can be an ideal solution for off-grid wind power desalination.

Graphical Abstract

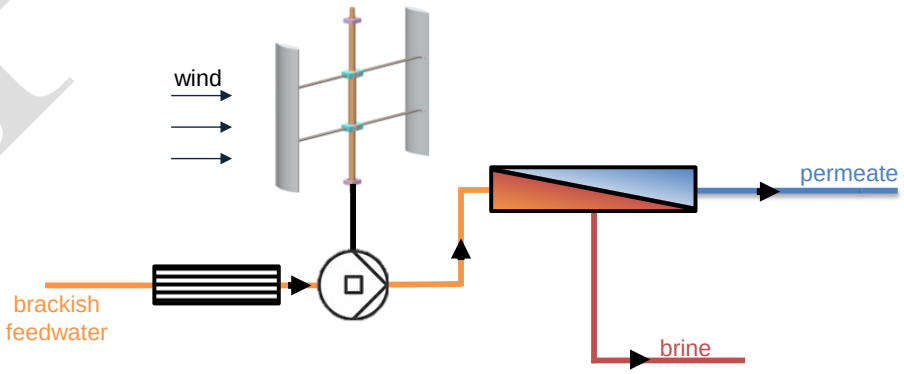

Nomenclature

A	=	swept area [m^2]
A_{mem}	=	membrane surface area [m^2]
BR	=	blockage ratio
c	=	blade's chord length [m]
c_f	=	feed flow concentration [ppm]
c_M	=	molar concentration [mol/l]
C_P	=	power coefficient
$C_{P,max}$	=	maximum power coefficient
d	=	pipe diameter [m]
h	=	blade's span [m]
i_{Hoff}	=	Van't Hoff dimensionless constant
J_v	=	flux of the water through the membrane [m/s]
k_f	=	overall feed-side mass transfer coefficient [m/s]
L_p	=	water permeability constant of the membrane [m^3/N·s]
$L_{p,eff}$	=	effective water permeability constant of the membrane [m^3/N·s]
N	=	number of blades
p	=	water pressure at the pump's exit [Pa]
p_{brine}	=	brine's pressure [Pa]
p_{min}	=	minimum pressure required [Pa]
Δp	=	pressure rise across the pump [Pa]
Δp_{mem}	=	pressure difference across the membrane [Pa]
Δp_{valve}	=	pressure difference across the valve [Pa]
Q_{brine}	=	brine flow rate [m^3/s]
Q_{feed}	=	feed flow rate [m^3/s]
Q_{per}	=	permeate flow rate [m^3/s]
r	=	recovery rate; Q_{per} / Q_{feed}
R	=	turbine's radius [m]
R_{gas}	=	ideal gas constant [J/K·mol]
Re	=	Reynolds number
$\overline{Re_c}$	=	chord-based average Reynolds number; $U_\infty \lambda c / \nu$
SEC	=	specific energy consumption [kWh/m^3]
SEC_{elec}	=	specific electrical energy consumption [kWh/m^3]
SEC_{mech}	=	specific mechanical energy consumption [kWh/m^3]
SEC_{wind}	=	specific wind energy consumption [kWh/m^3]
T	=	turbine torque [N·m]
T_{max}	=	turbine's max torque [N·m]
TP	=	transmembrane pressure [Pa]
TDS	=	total dissolved solids [ppm]
$\overline{TDS}$	=	time-averaged total dissolved solids [ppm]
U_∞	=	effective wind speed [m/s]
$\overline{U_\infty}$	=	average effective wind speed [m/s]
$U_{\infty,nom}$	=	nominal wind speed [m/s]
V_b	=	blade velocity [m/s]
$\dot{W}_{brine}$	=	brine hydraulic power [W]
$\dot{W}_{elec}$	=	desalination electrical power [W]
$\dot{W}_{hyd}$	=	net hydraulic power [W]
$\dot{W}_{shaft}$	=	shaft net mechanical power [W]

$\dot{W}_{\text{shaft,max}}$	=	shaft max mechanical power [W]
$\dot{W}_{\text{shaft,req}}$	=	shaft required mechanical power [W]
ε	=	chord to radius ratio; $\varepsilon \equiv c / R$
η_{pump}	=	pump relative efficiency
η_{sys}	=	overall system efficiency (wind to hydraulic)
$\eta_{\text{sys,avg}}$	=	average system efficiency
$\eta_{\text{sys,max}}$	=	maximum system efficiency
θ_w	=	feed water temperature [C^o]
λ	=	tip-speed ratio; $\omega R / U_\infty$
λ_{opt}	=	tip speed ratio at $C_{P,\max}$
ν	=	air kinematic viscosity [m^2/s]
$\Delta\pi$	=	osmotic pressure difference across the membrane [bar]
$\Delta\pi_{co}$	=	corrected osmotic pressure difference [bar]
ρ_a	=	air density [kg/m^3]
ρ_w	=	water density [kg/m^3]
σ	=	solidity; $\sigma \equiv Nc / R$
σ_{TDS}	=	TDS standard deviation
σ_ω	=	rotational speed standard deviation
ω	=	rotational speed [RPM]
$\bar{\omega}$	=	time-averaged rotational speed [RPM]
AM	=	American multi-bladed
BW	=	brackish water
D-WPD	=	direct wind-powered desalination
EC	=	electrical conductivity
HAWT	=	horizontal-axis wind turbine
HP	=	high pressure
HDPE	=	high density polyethylene
MSF	=	multi-stage flash
NLF	=	natural laminar flow
ppm	=	particles per million
PV	=	photo-voltaic
RO	=	reverse osmosis
Re	=	Reynolds number
SW	=	sea water
VAWP	=	vertical axis wind pump
VAWT	=	vertical axis wind turbine
WHO	=	world health organization

1 Introduction

The threat of global warming to the earth's ecosystem [1] has created a need for zero carbon emission systems, particularly for water supply and management [2,3]. This need is particularly acute for desalination, which has become a substantial share of the drinking and irrigating water in many countries [4,5]. Annually, it is estimated that the desalination process alone accounts for more than 400 million tons of carbon equivalent emissions [6]. Thus desalination must be rendered more sustainable, both ecologically and with regard to carbon emissions [7].

The two most widespread desalination technologies are thermally-based multi-stage flash (MSF) and membrane-based reverse osmosis (RO), with 17.5% and 69% of worldwide desalination capacity, respectively [8]. RO utilizes high-pressure pumps to overcome osmotic pressure in partially permeable membranes [9–11], but the energetic cost is substantial [7,12]. Significant energy must be invested to desalinate sea and brackish water from total dissolved solids (TDS) levels of 1,500-40,000 ppm to palatable water, determined by the world health organization to be less than 600 ppm [13].

The wind is a prominent energy source that can be used for low carbon-footprint desalination processes [14,15]. However, it is estimated that large-scale conventional wind-powered desalination plants, where the electricity and the desalination are two independent processes, can lose up to 40% of the useable wind power in generators, transmission, and pump motors [16–18]. These losses are even greater for small-scale systems. Although various systems and models were studied for direct electrical wind-RO desalination, i.e., without batteries or grid connection [19–25], the proposed systems have several critical disadvantages. For example, for small-scale systems, mechanical/electrical and electrical/mechanical conversion losses are excessive, resulting in significant losses of the useable wind power. Additionally, they demand high capital costs to construct, whereas expensive electrical systems and electronics elevate the system price, making them uneconomical at small scales or for private use [26–29].

The energetic losses described above motivate strongly in favor of the direct mechanical conversion of wind energy to pumping energy [30,31]. Since the American multi-bladed (AM) wind-pump is a widespread and well-understood system, able to produce relatively high pressures with its piston pump at ground level, it was naturally coupled mechanically to a desalination system. However, AM wind pumps have inherent limitations resulting in wind-to-hydraulic efficiencies between 4% and 8% [32]. Thus, it is no surprise that AM-driven reverse osmosis desalination systems attain low pumping and desalination efficacies [33–35]. Conversely, a study by Liu et al. [35] demonstrated a direct AM-driven reverse osmosis

desalination system with feedback control that can achieve efficiencies of up to 13%. However, high efficiency is only obtained for a negligible wind range. Thus, on average, system efficiency could not surpass 7% and was lower when the TDS feed flow level was altered.

In contrast to the decrease in the relevance of high-solidity horizontal axis wind turbines (HAWTs), that drive the AM pumps, interest in high-solidity vertical axis wind turbines (VAWTs) has surged due to advantages such as wind-direction insensitivity [36], low rotational speed and low noise emissions [37]. Those advantages are amplified for uncharacteristically large blade chord-to-radius ratios [38], where exceptionally low cut-in wind speeds of up to 1.5 m/s and exceptionally low rotational speeds can be achieved that further reduce noise emissions and the probability of bird strikes [39]. The mechanical integration of a VAWT with a pump produces what we refer to as a vertical axis wind pump (VAWP). Lift-based VAWPs [40] are favored over drag-based VAWPs [41] due to their higher aerodynamic efficiency [42]. Additionally, low-solidity VAWTs [43] suffer from low aerodynamic efficiency at low wind speeds and small scales operating at relatively low Reynolds numbers. Thus, for small-scale direct wind-powered desalination, high-solidity VAWPs are preferable.

The objective of this research is to experimentally evaluate the utility of a high-solidity, high-pressure vertical axis wind pump for brackish water desalination. To this end, a small-scale VAWT was constructed and mounted in a wind tunnel. The turbine shaft was interfaced directly with a positive displacement pump that was used to drive the brackish water through an RO filter. The paper is structured as follows: section 2 describes the experimental configurations; section 3 presents the result and discussion for the VAWT, the VAWP, and the D-WPD system; and section 4 summarizes the conclusions and outlook for direct wind-powered desalination systems.

2 Experimental Setup

Experiments were conducted in a blow-down wind tunnel with a 1 m × 1.9 m test section and a length of 3.65 m. The wind tunnel has a maximum speed of $U_\infty = 16\text{m/s}$, a relative standard deviation distortion of 1.4%, and a turbulence level of 0.5%. All experiments were performed at steady nominal wind speeds in the range: $2.8\,\text{m/s} \le U_{\infty,\text{nom}} \le 5.7\,\text{m/s}$. A high-solidity, two-bladed, H-rotor vertical axis wind turbine was constructed and mounted in the center of the test section (see Figure 1).

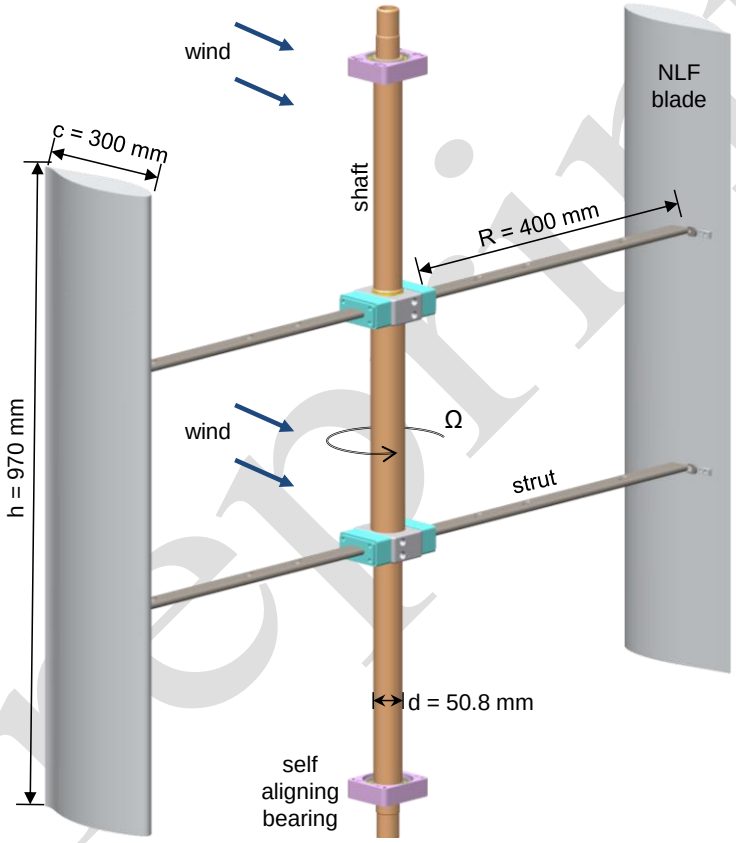

Figure 1: Schematic of the H-rotor vertical axis wind turbine showing its geometry and relevant dimensions.

2.1 Vertical Axis Wind Turbine

The turbine configuration employed in this study is based on a two-bladed H-rotor configuration and operates under the principle of dynamic stall (see Figure 1). Due to its low blade speeds, it has low noise emissions [37], a low risk of bird strikes [38], high torque and good self-starting capabilities [44]. It is comprised of a 50.8 mm shaft supported by two self-aligning ball bearings and two 21% thick natural laminar flow (NLF) blades [45] ($N = 2$, chord length $c = 300$ mm) that were connected to the shaft by struts (see Figure 1). The blades were

constructed with a span of $h = 970$ mm, ameliorating the generation of strong tip vortices, thus increasing its virtual aspect ratio. It was mounted in the center of the test section, located immediately downstream of the contraction. The turbine radius was $R = 400$ mm resulting in a swept area of $A \approx 0.8\text{m}^2$, a chord-to-radius ratio of $\varepsilon \equiv c/R = 0.75$, solidity of $\sigma \equiv Nc/R = 1.5$ and a blockage ratio of $BR \approx 41\%$. Due to the relatively high blockage ratio, wind tunnel corrections were implemented based on Kinsey and Dumas [46], leading to effective wind speeds in the range $4\,\text{m/s} \le U_\infty \le 8.5\,\text{m/s}$.

2.2 Turbine-Pump Interface

On the basis of performance estimation [38,40], a Hydra-Cell G03-E of a membrane-based positive displacement pump, with a nominal flow rate of 4.7 milliliters per revolution and a maximum pressure of 83 bars, was selected. The turbine shaft was connected to a Kistler 4502A1RAU (1±0.0015 Nm) dynamometer, which, in turn, was connected to the pump directly without any gearing. All mechanical connections were made using flexible couplings to accommodate misalignments. The feed water was pumped from a dedicated feed-water reservoir, placed at the pump level, and since no purification system was employed, the water was drained back in a closed loop. An HDPE piping, reinforced with aluminum, with a diameter of $d = 16$ mm was employed for the system.

The system performance was evaluated prior to interfacing with the desalination module, using a 27 bar (GEMU 543-S0) flow regulator valve to regulate the system's pressure (see Figure 2). The flow regulator was operated by a TTI CPX400DP programable power supply controller and via a dedicated LabVIEW® program. No correlation was observed between the turbine's performance and the angle phase between the turbine and the pump azimuthal angles.

2.3 Desalination System

Following the characterization of the wind-pump, the system was coupled directly to an RO desalination system (see Figure 2). The feed water used was synthetic brackish water comprised of desalted water mixed with 2.5, 5.0, and 10 g/L NaCl, which was drawn through a 5-micron Culligan CW5-BBS sediment filter. Although the brackish water in the Israeli desert is usually at the lower range of these TDS values [47], a relatively wide range was chosen to test the system robustness for various TDSs. The water was maintained at a constant temperature of $\theta_w = 25° \pm 1°$, and electrical conductivity (EC) temperature corrections were made for every measurement.

The water was then pressurized through a BW-2521 Max-Flow 2.5″×21″, anti-fouling brackish water RO desalination element, and the programable flow regulator was set at its brine exit. Since the permeate pressure at exit is atmospheric and the pressure drop at the permeate side was negligible due to the low feed flow/flux, the module feed in pressure and transmembrane pressure were considered identical in this study, $p \approx TP$. The permeate and the brine exiting the module were collected in two separate reservoirs to study the average response of the system. The reservoirs were placed on top of the feed-water reservoir to facilitate water reuse in subsequent experiments. Since the feed water was directly prepared under controlled conditions, there was no need for sand, granular activated carbon, activated carbon blocker, and other pre- and post-treatment filters.

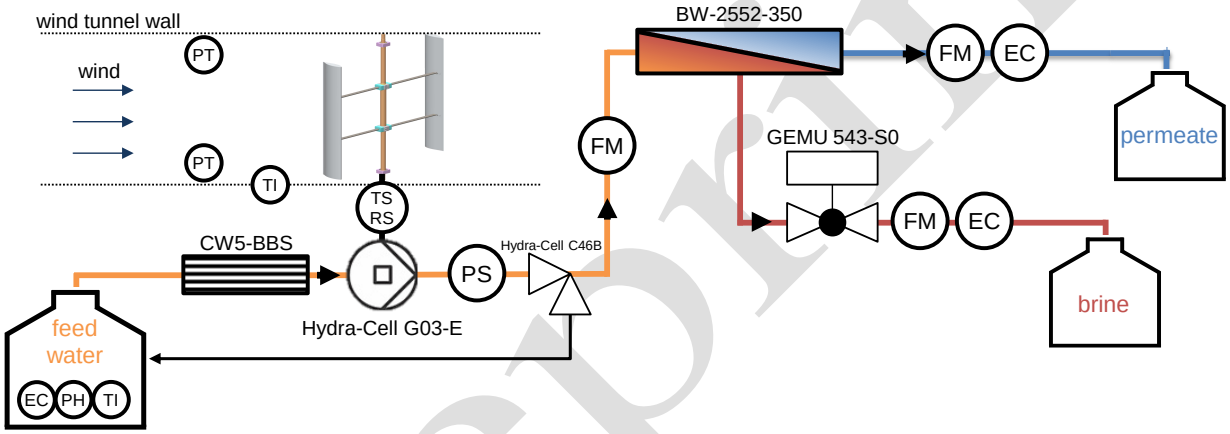

Figure 2: Schematic of the experimental wind-powered desalination system. Arrows indicate the flow direction. PS – pressure transducer; FM – flowmeter; EC - electrical conductivity meter; TS – temperature sensor; PH – PH meter; PT – pitot tube; TM – torque meter; RS – rotational speed sensor.

Figure 3 shows the feed-side pressure in the module as a function of Q_{brine}^2, where Q_{brine} being the brine flow rate for different experiments with four valve opening ratios. The result shows that an assumption of turbulent-mode pressure losses in the valve for all brine flow rates is valid and that the loss coefficients do not depend on the feed water's pressure or salinity. Thus, the pressure modeling can be formulated as two parallel restrictor systems, a valve, and a semipermeable membrane.

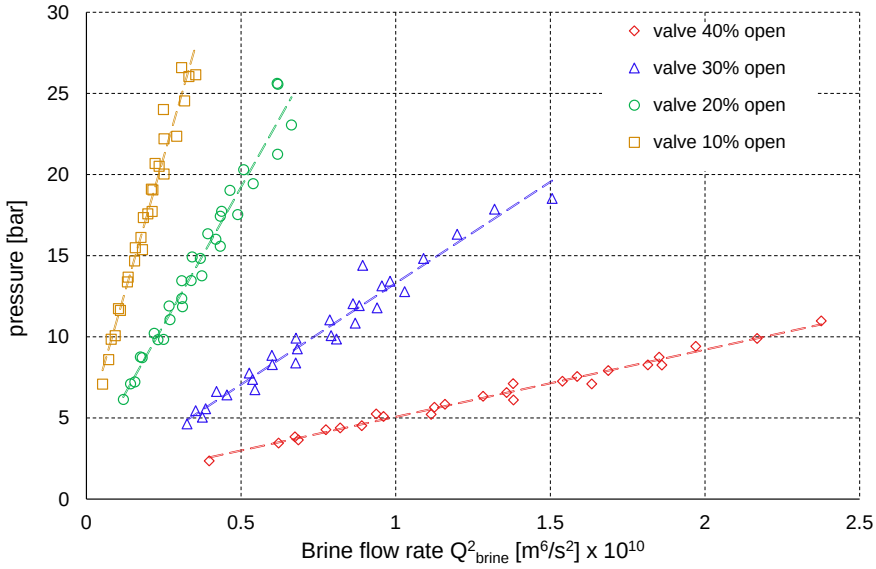

Figure 3: RO module inlet pressure, p, as a function of brine flowrate squared, Q^2_{brine}

2.4 Data Acquisition

Pressure was measured at the pump exit by a 40 ± 0.1 bar BD OEM 26.600, membrane-based pressure transducer. The flow rate was evaluated at the pump exit by a 0.5-16.5 liter/min, COMAC-Cal, flow-32, magnetic flowmeter. In addition, the flow rate was measured at the membrane's brine and permeate exits by two Badger Vision, 1005 2F66, 0.1-2.5 liter/min, flowmeters. HM Digital 716160 EC&TDS meters were used to determine the EC and ppm of the feed water, brine and permeate. The wind tunnel speed was monitored at 2 meters upstream of the turbine shaft for all experiments, employing two pitot-static probes connected to two low-pressure, 50 ± 0.3 Pascal Siemens QBM3020-1U, transducers. All the data were acquired and processed via a dedicated real-time LabVIEW® program. The complete dynamic response of the system during the experiment was obtained. For each experiment, a single control parameter was varied: wind speed or load, followed by a settling time. All system data were acquired for 60 seconds following steady-state conditions, defined as stabilization of the permeate TDS and ω. Steady-state conditions are defined as $\sigma_{\text{TDS}} / \overline{\text{TDS}} < 1\%$ and $\sigma_{\omega} / \bar{\omega} < 0.2\%$ for 60 seconds, where σ_{TDS} and σ_{ω} are the TDS and rotational speed standard deviation, correspondently, and $\overline{\text{TDS}}$ and $\bar{\omega}$ are the time-averaged TDS and rotational speed, correspondently.

3 Results and Discussion

3.1 Turbine and Wind-Pump Performance

The initial objective was to study the hydraulic load of the desalination system to the loads attainable by the turbine pump. Wind turbine efficiency is characterized by the power coefficient:

$$C_p \equiv \frac{\dot{W}_{\text{shaft}}}{\frac{1}{2}\rho_a A U_\infty^3} \tag{1}$$

where $\dot{W}_{\text{shaft}} = T\omega$ is the shaft power, T is the shaft torque, ω is the turbine's rotational speed and ρ_a is the air density. The 'pump's mechanical efficiency is defined as:

$$\eta_{\text{pump}} \equiv \frac{\dot{W}_{\text{hyd}}}{\dot{W}_{\text{shaft}}} \tag{2}$$

where $\dot{W}_{\text{hyd}}$ is the net hydraulic power:

$$\dot{W}_{\text{hyd}} = \Delta p Q_{\text{feed}} \tag{3}$$

where Δp is the pressure rise across the pump and Q_{feed} is feed flowrate through the pump. Thus, the overall system efficiency is obtained by simple multiplication, namely:

$$\eta_{\text{sys}} \equiv \eta_{\text{pump}} C_p = \frac{\Delta p Q_{\text{feed}}}{\frac{1}{2}\rho_a A U_\infty^3} \tag{4}$$

Note that a low hydraulic load causes the system to operate at low efficiency, while an excessive load arrests the turbine rotation, as demonstrated in [40].

Wind turbines are characterized by their performance map, namely C_P versus tip speed ratio, defined as:

$$\lambda \equiv \frac{\omega R}{U_\infty} \tag{5}$$

The performance map is e generated by varying the load imposed on the turbine shaft as described in [38], and the turbine employed here operates in the range of $0.8 \le \lambda \le 1.8$.

For each experiment, the turbine was unloaded (regulator valve fully open) to maximum rotational speed and then gradually loaded (new valve setting) until the total arrestation. Data were acquired under steady-state conditions at each valve setting, as described in section 2.4. Figure 4 and Figure 5 show selected examples of the turbine performance (C_P versus λ) and the pump hydraulic efficiency (η_{pump} versus λ), respectively. The maximum power coefficients, in the range of $0.21 \le C_{P,\max} \le 0.24$, are seemingly low, especially when compared to

commercially-available large-scale VAWTs [48]. It should be noted, however, that these results are, in fact, highly competitive with small-scale turbines since the operational Reynolds numbers are very low. The chord-based average Reynolds number for a VAWT is commonly defined as:

$$\overline{Re_c} = \frac{V_b c}{\nu} = \frac{\lambda U_\infty c}{\nu} \tag{6}$$

where ν is the kinematic viscosity of the air and V_b is the blade velocity. Note that the variation in our data from $\overline{Re_c} = 0.9\times10^5$ ($U_\infty = 4.2$ m/s) to $\overline{Re_c} = 1.5\times10^5$ ($U_\infty = 7.2$ m/s) at $C_{P,\max}$ produced a 17% increase in C_P. This increase was not unexpected because significant increases in aerodynamic efficiency occur over this Reynolds number range [49,50]. Furthermore, based on unique dynamically scaled experiments of Miller et al. [51,52], more than 50% increases are attainable when $\overline{Re_c} > 10^6$.

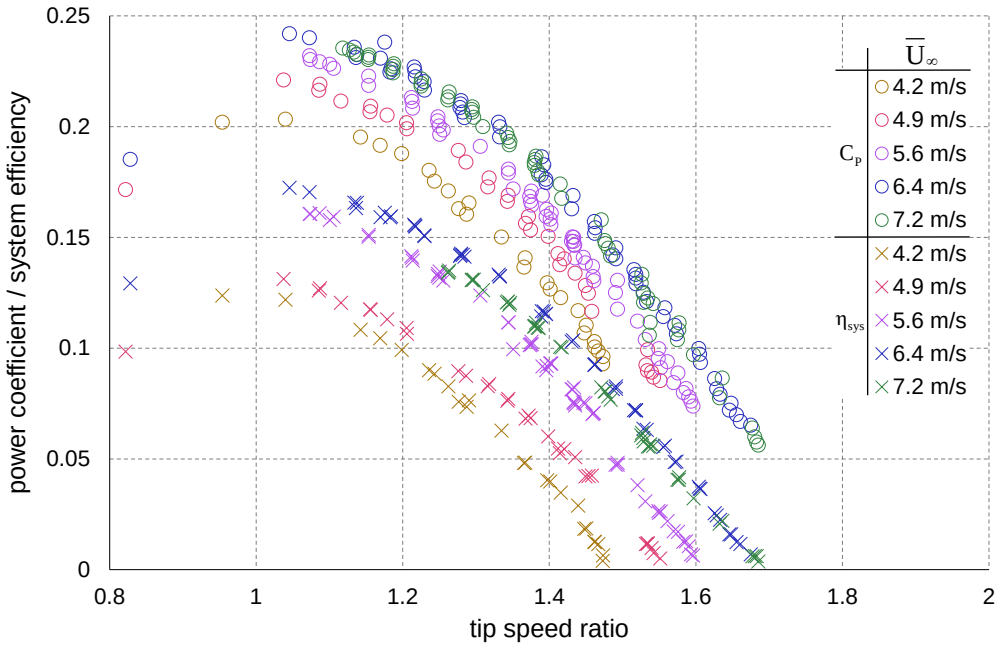

Figure 4: Turbine power coefficient as a function of tip-speed ratio for different wind tunnel speeds.

As shown in [40], the efficacy of the turbine in converting wind energy to mechanical power is essentially independent of the load applied, electric, mechanical, or hydraulic (pump). However, a hydraulic load, or other quasi-linear loads devoid of a rotational speed controller, are able to operate only in stable turbine-load λs. As long as the $T < T_{\max}$, this operation regime exists for all tip speed ratios higher than the maximum efficiency TSR, $\lambda \geq \lambda_{opt}$, where λ_{opt} is

the tip speed ratio at $C_{P,\max}$, as can be seen in Figure 4, where higher λ values yield lower efficiencies. Additionally, subject to the load applied, several stable operational λs may appear at the range of $\lambda < \lambda_{opt}$. However, we generally avoid operation in this tip speed ratio regime, $\lambda < \lambda_{opt}$, as a non-stable operation zone for a VAWP.

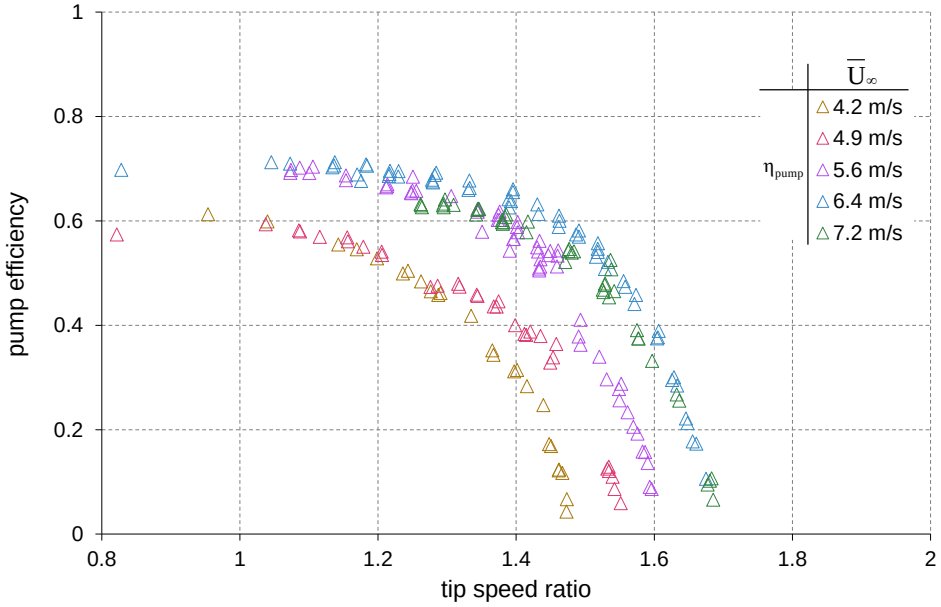

Figure 5: Pump efficiency as a function tip speed ratio for different wind tunnel speeds.

As higher wind speed results in more considerable C_P, an increase in the system efficiency of the VAWP is also noticed. However, the increase in η_{sys} is higher than the increase of the C_P due to an additional increase in the pumping efficiency (see Figure 5) of up to 18%, yielding a mechanical to hydraulic efficiency of up to $\eta_{pump} = 71\%$. This increase is due to the lower relative residual torque of the pump. For similar λ, higher wind speeds yield higher rotational speeds and torque, increasing Q_{feed} and p. Due to the increase in torque, the system experiences lower relative residual torque, yielding higher hydraulic efficiencies at higher wind speeds. In addition, since the pump operates at relatively lower rotational speeds and loads than those set in its design, increasing the pump rotational speed and pressure may increase its efficiency.

In this section, we considered the hydraulic efficiency of the D-WPD system as the main parameter to study the turbine's efficacy. However, a desalination system's efficacy is not rated by its hydraulic efficiency but, generally, by the ratio of permeate flow rate to electrical power

input $Q_{\text{per}} / \dot{W}_{\text{elec}}$ [kWh/m^3], also referred to as specific energy consumption (SEC). Conversely, multiplying the hydraulic efficiency, η_{sys}, by the recovery rate, $r \equiv Q_{\text{per}} / Q_{\text{feed}}$, yields the net energy per permeate volume. Thus, to increase our permeate production, we need to optimize both the hydraulic efficiency and the recovery rate for a given RO module. Therefore, although η_{sys} it is not the main parameter to optimize, it is crucial for optimizing the entire desalination system performance.

3.2 Desalination System Performance

Following the wind-pump experiments, the system was connected to a desalination system, as described in section 2.3. The system performance was analyzed for three different feed NaCl concentrations, namely $c_f = 2{,}500$ ppm, 5,000 ppm and 10,000 ppm. Two types of experiments were performed for each concentration: (i) the wind speed was maintained constant, and the load was varied by changing the feed pressure valve position; and (ii) the valve position was maintained constant while the wind speed was varied. Accordingly, the influence of the wind speed, valve load, or NaCl concentration on the system's performance and various parameters were analyzed.

3.2.1 Feed Flow Response

Figure 6 shows the feed flow rate, Q_{feed} as a function of the rotational wind speed ω. The data showed that the pump displacement is $\partial Q_{\text{feed}} / \partial \omega \approx 3.8$ ml/rev for a system operating at $p > 3$ bar, whereas for lower pressures, the displacement is higher, up to 5.1 ml/rev. The data points within the shaded area are for feed water concentrations of 10,000 ppm and should be ignored due to activation of the pressure relief valve (set at ~27 bars) in these conditions. Constant displacement per revolution corresponds to the pump working as an ideal positive displacement pump. Regardless of the turbine rotation speed, the feed flow would simply be a linear function of the turbine rotation speed. If, further, a constant tip speed ratio can be maintained for different wind speeds, the feed flow would also become a linear function of U_∞ .

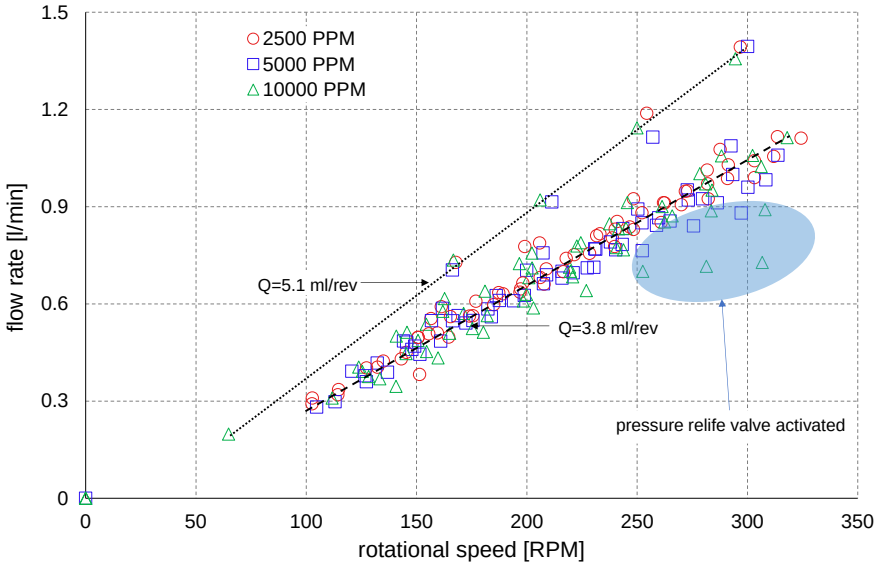

Figure 6: feed water flow rate, Q_{feed} as a function of rotational speed, ω for various feed TDS.

For a system operating at pressures of $p > 3$ bar, the attained pump displacement was

$$\partial Q_{\text{feed}} / \partial \omega \approx 3.8 \text{ ml/rev}.$$

3.2.2 Pressure Response

Figure 7 (a-c) shows the pressure at the RO module inlet as a function of ω for the different salinities. Each panel displays the pressures measured in eight separate experiments. Four experiments were performed at constant wind speeds while increasing valve load, resulting in a pressure increase accompanied by a reduction in λ, thus reducing the relative feed flow rate (marked as circles). The additional four experiments are at a constant valve position while increasing the wind speed, resulting in an increasing feed flow rate and the system's pressure (marked as triangles).

All plots indicate that the system response is independent of the varied parameter. This is a welcome result because it implies that both the pressure and flow rate show negligible hysteresis, an adverse feature of mechanical systems. An essential and valuable conclusion that can be drawn from Figure 7 is that the pressure versus rotational speed relationship is linear, standing in contrast to the typical hydraulic system characteristics, where $\Delta p \propto Q^2$ [53]. The linearity of the pressure with the rotational speed resembles the assumptions made in [40] for a VAWP-desalination system.

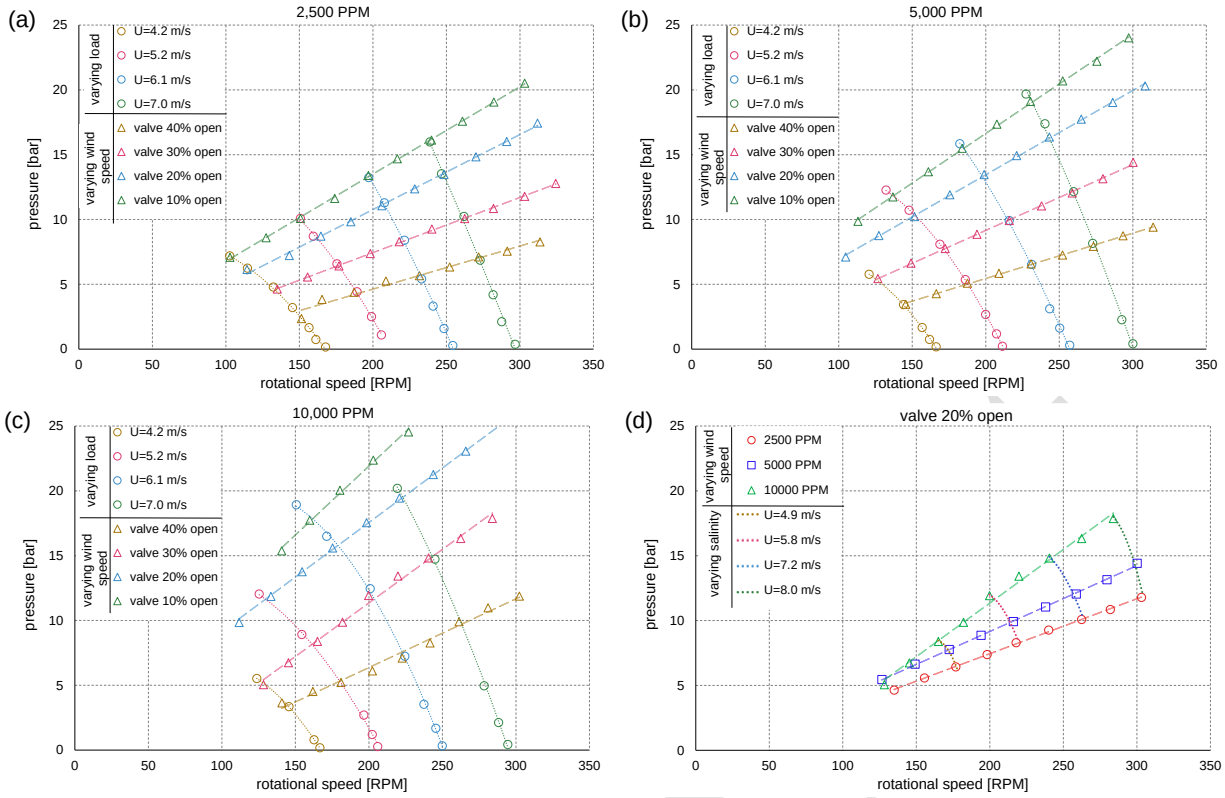

Figure 7: (a-c) RO module inlet pressure, P as a function of the rotational speed, ω for feed TDS of (a) 2,500 ppm (b) 5,000 ppm (c) 10,000 ppm for various valve settings and wind speeds; and (d) constant valve setting, 20%, for various salinities and wind speeds.

3.2.3 Influence of Salinity on Performance

In contrast to the wind-pump system, where water composition has a negligible impact on performance, both the pressure and the pressure gradient $\partial P / \partial \omega$ depend on salinity (see Figure 7 (d)). The flux of the water through an ideal salt-rejecting membrane, J_v, is usually [54] defined as:

$$J_v = L_p \left(\Delta p_{\text{mem}} - \Delta \pi \right) \tag{7}$$

where L_p is the membrane's water permeability constant, Δp_{mem} is the pressure difference across the membrane and $\Delta \pi$ is the osmotic pressure difference across the membrane. Due to the increase in the water salinity, the osmotic pressure increases, as defined by Van't Hoff:

$$\pi = i_{\text{Hoff}} c_M R_{\text{gas}} \theta_w \tag{8}$$

where i_{Hoff} is the dimensionless Van't Hoff constant (for NaCl, $i_{\text{Hoff}} = 2$), c_M is the molar concentration and R_{gas} is the ideal gas constant. From eqn. (8) we can calculate the osmotic

pressures of the feed water, namely $\pi \approx 2.1$ bar, 4.2 bar and 8.4 bar for salinities of 2,500 ppm, 5,000 ppm and 10,000 ppm, respectively. As shown by Lee and Kim [55], for NaCl concentration less than 1.5 mol/L, the deviation from Van't Hoff osmotic pressure is negligible, thus, those approximations are justifiable. However, this is a simplified definition, as will be further elucidated, eqn. (8) describes the main physical reasoning for pressure differences corresponding to different salinities.

To explain the observed pressure-rise at a constant RPM with increasing salinity, consider a hypothetical case where the turbine operates at $C_P < C_{P,\max}$, corresponding to $\lambda > \lambda_{\max}$. Since we use a positive displacement pump, we can assume (see Figure 6), that:

$$Q_{\text{feed}} \propto \omega \tag{9}$$

Based on Figure 3, we can assume turbulent losses, thus:

$$\Delta p \approx \Delta p_{\text{valve}} \propto Q_{\text{brine}}^2 \tag{10}$$

where Δp_{valve} is the pressure-loss across the valve and equel to Δp_{brine}. Since $Q_{\text{brine}} = Q_{\text{feed}} - Q_{\text{per}}$ and $Q_{\text{per}} = J_v A_{\text{mem}}$, where A_{mem} is the membrane surface area, integration of equations (7) to (9) into eqn. (10), results in:

$$\Delta p \propto \left(Q_{\text{feed}} - A_{\text{mem}} L_p \left(\Delta p_{\text{mem}} - i_{\text{Hoff}} \Delta c_M R_{\text{gas}} \theta_w \right) \right)^2 \tag{11}$$

Since $\Delta p \approx \Delta p_{\text{valve}}$, we obtain a nonlinear equation, where an increase in the feed salinity, c_M, produces a pressure rise.

Additionally, the increase in salinity reduces the permeate production and increases the required shaft power, as denoted by eqn. (7) and (3), respectively. Assuming that the increase in the required shaft power is lower than the maximum available turbine shaft power:

$$\Delta p Q_{\text{feed}} = \dot{W}_{\text{shaft,req}} \leq \dot{W}_{\text{shaft,max}} = \tfrac{1}{2} \rho_a A U_\infty^3 C_{P,\max} \tag{12}$$

an increase in the salinity will increase the power coefficient, thus increasing the system's efficiency. This can be observed in Figure 8, where an increase in c_f at $U_\infty > 6.1$ m/s increases both C_P and η_{sys}. However, as demonstrated later, at lower wind speeds, an increase in salinity can arrest the turbine because the turbine cannot match the additional load produced by the desalination system, $\dot{W}_{\text{shaft,req}} > \dot{W}_{\text{shaft,max}}$.

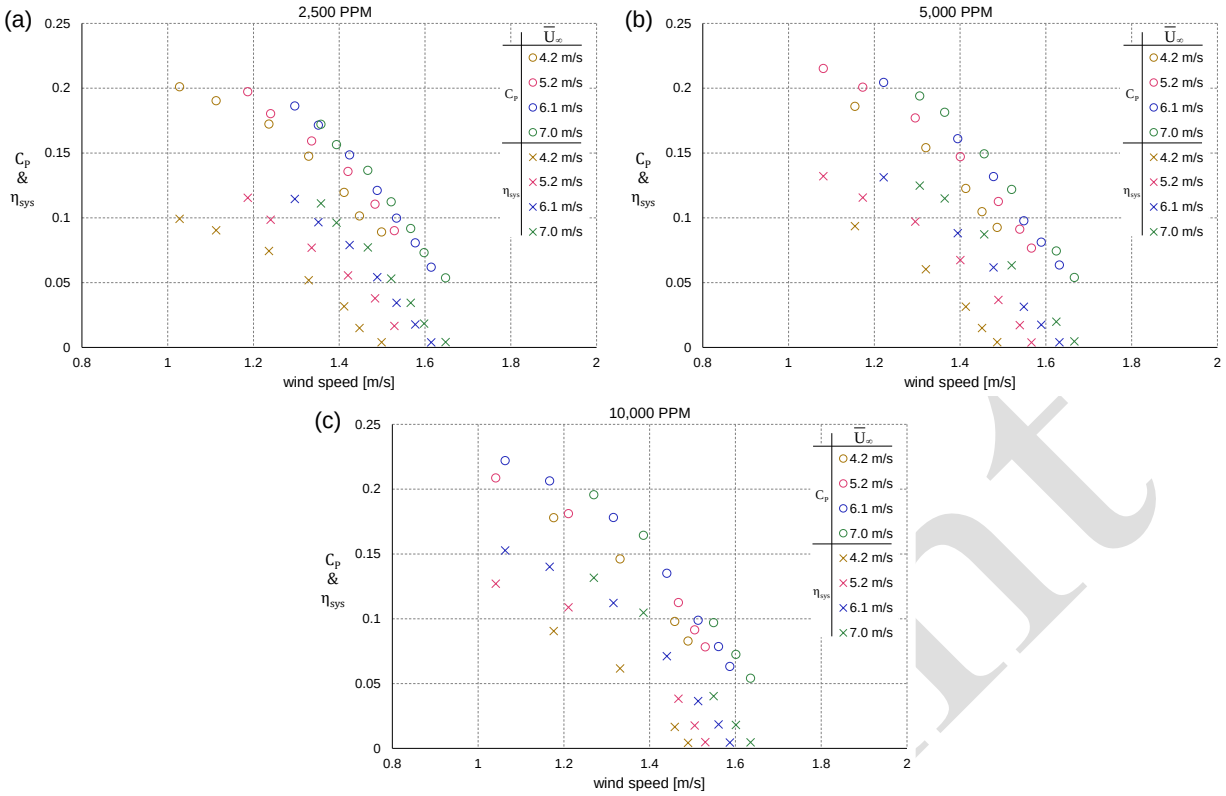

Figure 8: Turbine power coefficient (circles) and hydraulic efficiency (axes) as a function of λ for various wind speeds for the various feed water TDS.

3.2.4 Permeate Production

Figure 9 (left) presents the permeate flow and recovery rates as a function of inlet pressure. Using linear least-squares approximation (see eqn. (8)), we obtain that the osmotic pressures of the feed water are $\pi \approx 2.1$ bar, 4.2 bar and 8.4 bar for salinities of 2,500 ppm, 5,000 ppm, and 10,000 ppm, respectively. As estimated, the osmotic pressure obtained from the data matches the calculated osmotic pressure, with up to a 5% error (Figure 9 (left)). The non-linearity observed in instances of $p \to \Delta\pi$, are due to the relatively large permeation of the salt as opposed to the relatively slow permeation of the water, making the permeate more saline, at $p \to \Delta\pi$.

As obtained from Figure 9 (right), the slope of Q_{per} versus $p - \Delta\pi$ decreases with the increase in c_f, deviating from eqn. (7), with a constant linear slope, L_p. There are two main reasons for the change in the slope: (i) membrane swelling; and (ii) increased osmotic pressure due to concentration polarization. In the first instance, increased salinity is known to cause an osmotic deswelling, reducing the membrane permeability [56]. Additionally, for a given feed flow rate, permeate flux increasing with feed pressure exacerbates concentration polarization,

progressively raising the osmotic pressure at the membrane surface above that of the feed $\Delta\pi$. This results in a corrected osmotic pressure difference $\Delta\pi_{co}$ that should be used in eqn. (7), which varies with the permeate flow as $\Delta\pi_{co} \approx \Delta\pi \exp\left(J_v / k_f\right)$, where k_f the overall feed-side mass transfer coefficient [57,58]. When J_v / k_f is not excessively large, the exponent may be expanded as $\Delta\pi_{co} \approx \Delta\pi\left(1+J_v / k_f\right)$, yielding the corrected approximation for the flux of the water through the membrane:

$$J_v = L_p\left(\Delta p - \Delta\pi_{co}\right) = L_p\left(\Delta p - \Delta\pi - \Delta\pi\frac{J_v}{k_f}\right) \tag{13}$$

and hence the effective permeability constant:

$$L_{p,\text{eff}} = \frac{L_p}{1+L_p\dfrac{\Delta\pi}{k_f}} \tag{14}$$

The correction expressed in eqn. (14) shows that, as c_f and thus $\Delta\pi$ increase, the slope of Q_{per} versus p decreases, as observed.

Figure 9 (left) also shows that, for a constant salinity and pressure, higher recovery rates are obtained for slightly lower Q_{per} values. Here, increasing the feed flow rate by increasing wind speed and reducing the restriction of the valve results in a lower recovery rate at comparable pressures.

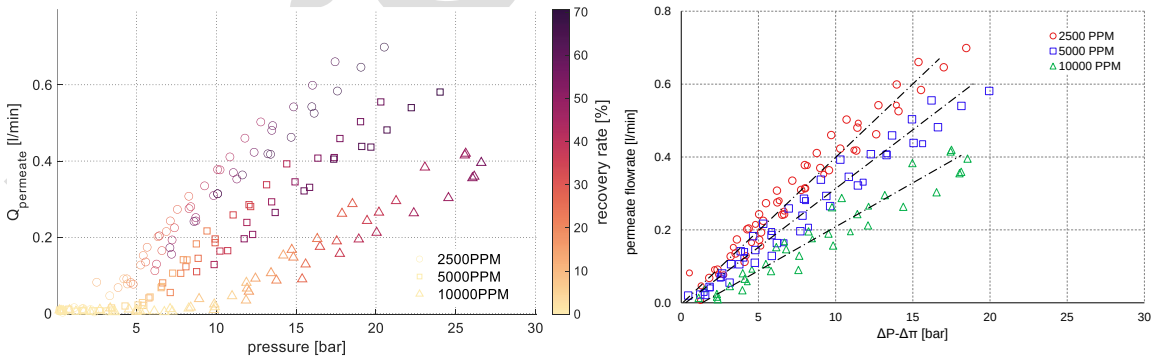

Figure 9: Permeate flow rate as a function of (left) inlet pressure, p, and recovery rate; and (right) $p-\Delta\pi$, for all experiments conducted. Dashed-doted lines represent linear interpolation of the data for every c_f.

3.2.5 Salt rejection

Figure 10 presents the steady-state permeate TDS and corresponding salt rejection attained by the system as a function of the membrane pressure for all experiments conducted. For $c_f \leq 5{,}000$ ppm, all the permeate TDS are below the maximum TDS for potable water recommended by the World Health Organization (WHO) [13]. For c_f = 10,000 ppm, the allowed TDS values were obtained for pressures $p \geq 12$ bar, approximately 1.5 times the osmotic pressure difference. From Figure 10 (right), we see that the salt rejection stabilizes for $P \geq 2\Delta\pi$. However, the membrane exhibits a reduction in the rejection rate ($c_f \leq 5{,}000$) when the pressure is higher, yielding higher recovery rates and a reduction of the brine flow. This decrease is due to enhanced concentration polarization, where the salt mass transfer cannot keep up with the salt convection towards the membrane with the transmembrane flow of water. This effectively increases the salt concentration at the upstream surface of the membrane, in the same manner as $\Delta\pi_{co}$, exponentially enhancing the salt permeation and increasing permeate salinity.

It must be stressed that, following initiation, at cut-in speeds (cut-in), the pump pressure increases to $\Delta\pi \leq p <\sim 1.2\Delta\pi$, and the system experiences a long transient process where permeate TDS values are initially high and slowly drop to the values presented in Figure 10 (left). The obtained permeate TDS values shown in Figure 10 (left) are then the steady-state TDS values obtained after the transient decrease of the TDS. The reason for the transient is that as the pressure builds up to exceed the osmotic pressure, the diffusion of salt through the membrane, which is largely independent of the water flow, is at first significant compared with the flow of water, resulting in a higher salt concentration in the permeate. Consequently, a field system operating average wind speeds yielding pressures of $\Delta\pi \leq p \leq 1.2 \cdot \Delta\pi$, would produce saltier permeate than presented in Figure 10. Since the transient process can have a significantly adverse effect on permeate salinity, it would be beneficial to integrate a minimal pressure valve upstream of the filter with $p_{min} \approx 1.2 \cdot \Delta\pi$.

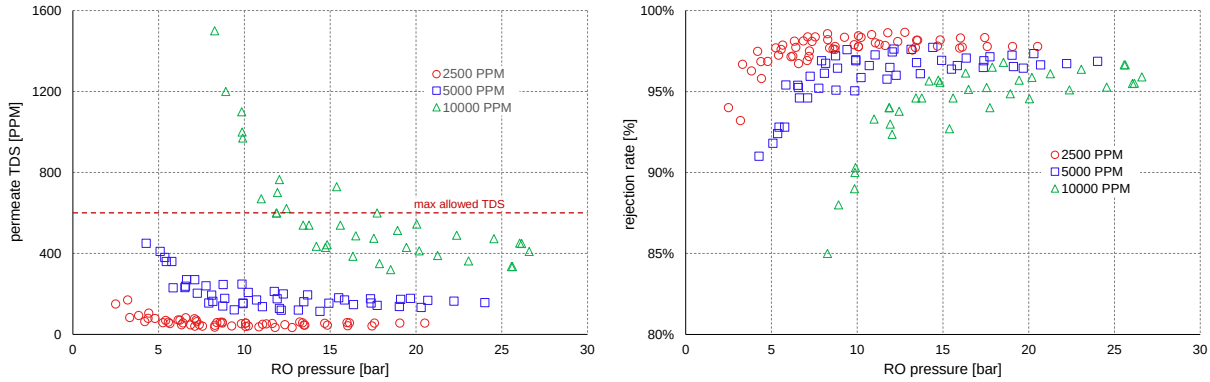

Figure 10: (Left) Permeate TDS; and (right) Salt rejection, as a function of inlet pressure, p, for all experiments conducted

3.3 Stand-Alone System Study

The influence of wind speed and permeate salinity was studied for a system at a constant valve setting (10% open) to determine the system's performance under typical field conditions. Measurements were made for commonly-encountered wind speeds, namely $4.2\,\text{m/s} \le \overline{U_\infty} \le 8.3\,\text{m/s}$ and for the three different feed NaCl concentrations, namely $c_f = 2{,}500$ ppm, 5,000 ppm, and 10,000 ppm.

3.3.1 Influence of Wind Speed on Performance

Figure 11 shows the influence of wind speed and permeate salinity on four system parameters, namely: (i) daily permeate flow, (ii) recovery rate, (iii) permeate TDS, and (iv) system efficiency. The results show that at an average wind speed of $\bar{U}_\infty \approx 7.7$ m/s, the system produces a daily yield of $Q_{\text{per}} \ge 0.5\,\text{m}^3/\text{day}$. Note, however, that this is a small laboratory-scale system with a swept area of $0.8\,\text{m}^2$ and that the yield increases linearly with the swept area. Moreover, an additional increase in permeate production can be expected due to an increase in system efficiency, as mentioned in section 3.1. From dimensional analysis, at the average wind speeds, increasing the swept area by a factor of 15, to 12 m^2, will result in a daily yield in the range $7.5\,\text{m}^3/\text{day} \le Q_{\text{per}} \le 13.25\,\text{m}^3/\text{day}$, depending upon the salinity of the feed water. For moderately low average wind speed of $\bar{U}_\infty \approx 5.0$ m/s, we can expect a yield in the range $2.1\,\text{m}^3/\text{day} \le Q_d \le 3.7\,\text{m}^3/\text{day}$. Furthermore, additional optimization can be made by varying system average operational pressures and feed flow for each salinity.

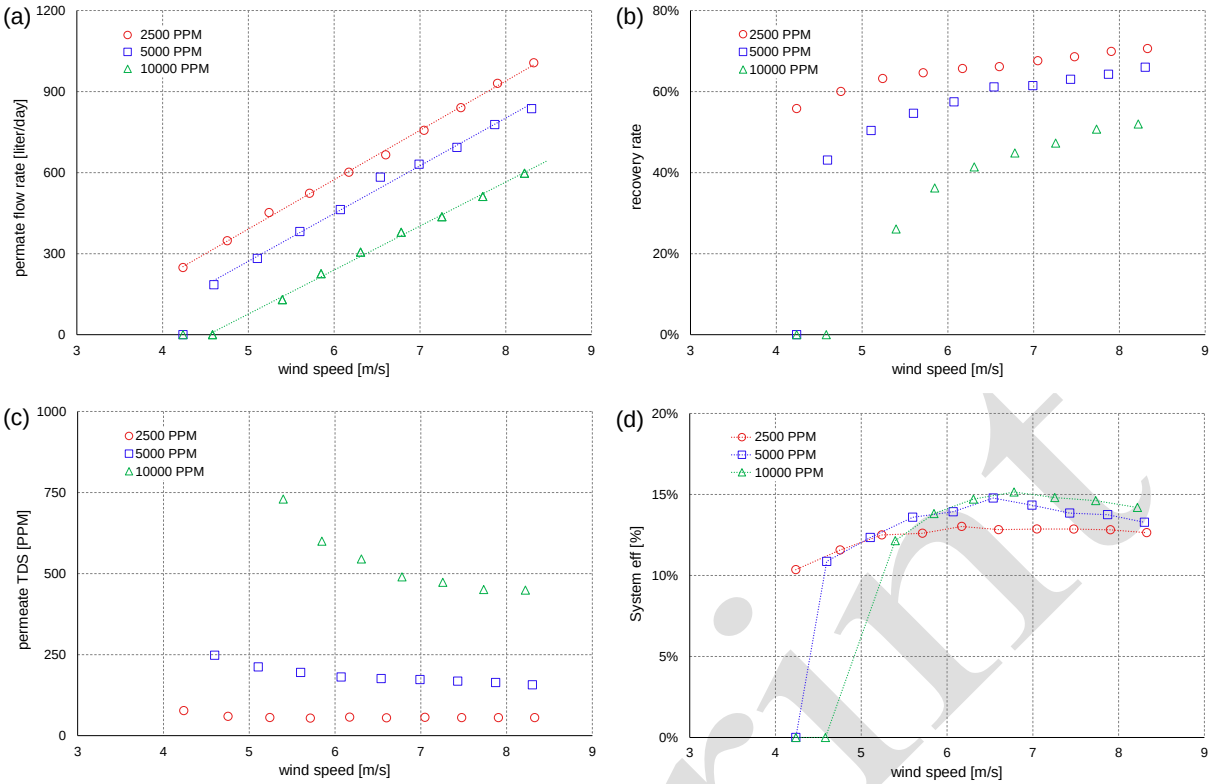

Figure 11: (a) Daily permeate flow, (b) recovery rate, (c) permeate TDS, and (b) system efficiency as a function of U_∞ for valve at a constant opening rate of 10%

The acquired data also indicate a linear correlation between the permeate production and the wind speed. We can derive this relationship based on previous data, namely: $Q_{\text{per}} \propto \Delta p$ (see Figure 9) and $\Delta p \propto \omega$ (see Figure 7), yielding $Q_{\text{per}} \propto \omega$. Since $\omega \propto \lambda U_\infty$, under the approximation that $\lambda \approx \text{const}$, we can deduce that:

$$Q_{\text{per}} \propto U_\infty \tag{15}$$

as confirmed in Figure 11 (a). This linear relationship between Q_{per} and U_∞ is valid for all salinities. Under these assumptions, we also note that:

$$p \propto U_\infty \tag{16}$$

Additionally, from eqns. (9) and (11), we can deduce that the slope of $p = f(\omega)$ increases with the increase in salinity, as shown in Figure 7 (d).

Again, assuming that $\lambda \approx \text{const}$, from eqns. (1) we gain that:

$$\dot{W}_{\text{mech}} \propto U_\infty^3 \tag{17}$$

and from eqns. (15) and (16), we can show that:

$$\Delta pQ = \dot{W}_{\text{hydra}} \propto U_\infty^2 \tag{18}$$

Finally, assuming a constant pump efficiency, we can develop the following system efficiency correlation:

$$\eta_{\text{sys}} \propto C_P / U_\infty \tag{19}$$

showing that the system's efficiency decreases with increasing wind speed. This result matches the obtained data from Liu et al. study [35]. In contrast, Figure 11 (d) denotes that increasing wind speed for a system with a constant salinity and valve settings first increases η_{sys} followed by a continuous plateau of the system efficiency, and this runs counter to our expectations shown in eqn. (19).

There are three main reasons for the almost constant efficiency of the system. First, significant increases in aerodynamic efficiency occur over this Reynolds number range, as discussed in section 3.1. This increase in wind speed brings about an increase in C_P, which violates the assumption expressed in eqn. (17). The assumptions expressed in eqns. (17) to (19) are only valid for a large-scale system where Reynolds number effects are small and the pump efficiency is assumed to be constant. Second, the pump efficiency increases markedly with increasing wind speed, as discussed in section 3.1, and therefore sets in contrast to the assumption in (18). This is because the relative residual torque is lower at increased rotational speeds, and the pump operates closer to its design conditions. Third, the approximation $p \propto \omega$ (based on Figure 7), is simply a local approximation of the pressure response, where the correct function is in all probability $p \propto \omega^y$ where y is a constant $1 < y < 2$, yielding a corrected correlation of the desalination efficiency:

$$\eta_{\text{sys}} \propto C_P \cdot U_\infty^{y-1} \tag{20}$$

On the other hand, the inverse relationship between the wind speed and η_{sys} can also arrest the turbine at low wind speeds since $\dot{W}_{\text{hydra}} > \eta_{\text{sys, max}} \cdot \left(\tfrac{1}{2} \rho_a A U_\infty^3 \right)$. Thus, a trade-off exists between increased wind-speed range and greater efficiencies at higher wind speeds – as anticipated by the model developed in [40].

In summary, the net result is an almost constant system efficiency of $12.5\% < \eta_{\text{sys}} < 15\%$ for a wide range of wind speeds and salinities. Notwithstanding the small scale of the system, these are remarkably high efficiencies. However, it is clear that far greater system efficiencies can be achieved on up-scaled systems where the characteristic blade Reynolds numbers are $\geq 10^6$ and pump efficiencies are optimized.

3.3.2 Energy Recovery

Although the system does not contain an energy recovery device (ERD), the estimated power available from the brine flow was calculated and presented in Figure 12. This power can be employed to produce electricity using a micro-Pelton wheel or a regeneration pump for irrigation or further pumping. The available power in the brine, $\dot{W}_{\text{brine}}$, is defined as:

$$\dot{W}_{\text{brine}} \equiv p_{\text{brine}} Q_{\text{brine}} \approx p(1-r) Q_{\text{feed}} \tag{21}$$

Since P and Q increase approximately linearly with the wind speed, from eqns. (15) and (16), we obtain that the available power in the brine is $\dot{W}_{\text{brine}} \propto U_{\infty}{}^{2}(1-r)$. Since turbine power increases with U_{∞}^{3}, with constant C_P a reduction in the relative available energy from wind energy is observed (Figure 12 (left)). We obtain from eqn. (21) that at higher salinities, where the system experience lower recovery rates, $\dot{W}_{\text{brine}}$ will be higher, as shown in Figure 12. Thus, a system that produces lower permeate production due to low recovery rates can increase its efficacy with the use of ERDs.

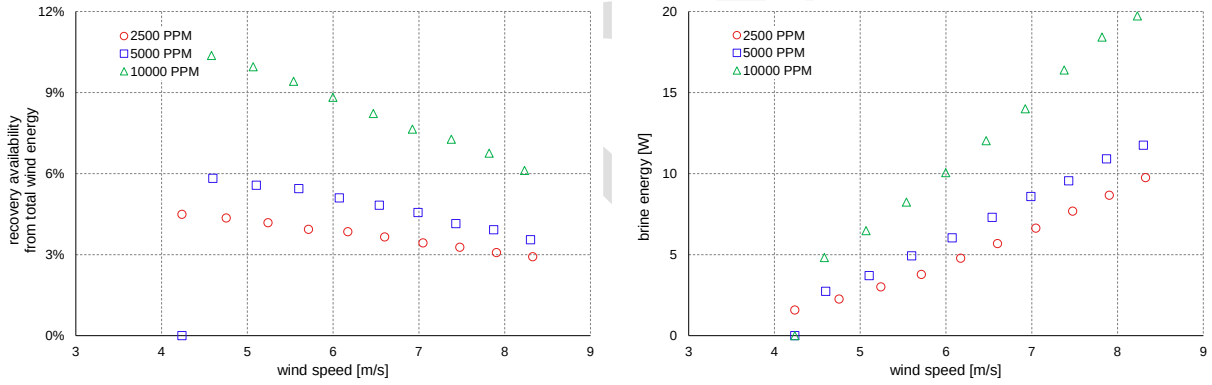

Figure 12: Available Power for energy recovery as a function of wind speed (left) relative available energy from wind energy; and (right) power in watts.

3.3.3 Specific Energy Consumption

Generally, desalination systems are not measured by their efficiency, but rather by their energetic efficacy, also known as specific energy consumption (SEC), defined as the energy required in kWh to produce one cubic meter of permeate. SEC is commonly defined by the electric energy, $\dot{W}_{\text{elec}}$, supplied to the RO pumps and supporting systems. However, in our case, no electricity is supplied by the system. Therefore, the definition of SEC was adjusted to

overcome this difference. The compatible SEC of a direct desalination system is defined by the mechanical energy supplied to the pump, $\mathrm{SEC}_{\mathrm{mech}}$, and defined as:

$$\mathrm{SEC}_{\mathrm{mech}} = \frac{\dot{W}_{\mathrm{shaft}}}{Q_{\mathrm{per}}} \cdot 2.78 \cdot 10^{-7} \left[\frac{\mathrm{kWh}}{\mathrm{m}^3} \right] \tag{22}$$

In addition, since the system is driven directly by wind, we define the specific wind energy consumption,

$$\mathrm{SEC}_{\mathrm{wind}} = \frac{½ \rho_a A U_\infty^3}{Q_{\mathrm{per}}} \cdot 2.78 \cdot 10^{-7} \left[\frac{\mathrm{kWh}}{\mathrm{m}^3} \right] \tag{23}$$

where $½ \rho_a A U_\infty^3$ is the gross available wind power.

Figure 13 shows $\mathrm{SEC}_{\mathrm{wind}}$ (left) and $\mathrm{SEC}_{\mathrm{mech}}$ (right) as a function of wind speed and c_f, for a system with the parameters described in section 3.3.1. Wind energy per cubic meter of 3.5 to 7 kWh of permeate is required for c_f of 2,500 ppm and 5,000 ppm, respectively for wind speeds $U_\infty \leq 8$ m/s. For 10,000 ppm, higher energy input is required of up to 13.5 kWh of wind power for wind speeds of $5.4 \text{ m/s} \leq U_\infty \leq 8$ m/s.

In order to compare the system energy demand, per cubic meter of permeate, to conventional small to medium-scale BW desalination systems, we can calculate the wind and electrical energy required if the turbine was to produce electricity feeding these desalination plants. First, we calculate the maximum power production of the wind turbine by extracting the maximal power coefficient at each wind speed from Figure 4. Next, we assume that specific electrical energy consumption, $\mathrm{SEC}_{\mathrm{elec}}$, of 0.8 to 2.5 kWh/m^3 for the BW desalination process with a salinity of 2 g/L up to 10 g/L, with no ERD [59–62], indicated by the shaded area in Figure 13, right. Finally, we assume a total electrical/mechanical transmission efficiency of 0.8. Accordingly, we can estimate the wind energy required for a conventional BW desalination plant powered by a small-scale VAWT, indicated by the shaded area in Figure 13, left. The data points fall mainly within the shaded area and indicate that our mechanically simple system is competitive even with optimized conventional wind-powered desalination systems. Note that our conservative assumptions can be improved by increasing the permeate flow through system optimization or implementing an ERD. The competitiveness of the D-WPD system is further demonstrated by a detailed comparison to past wind power desalination systems in the next section.

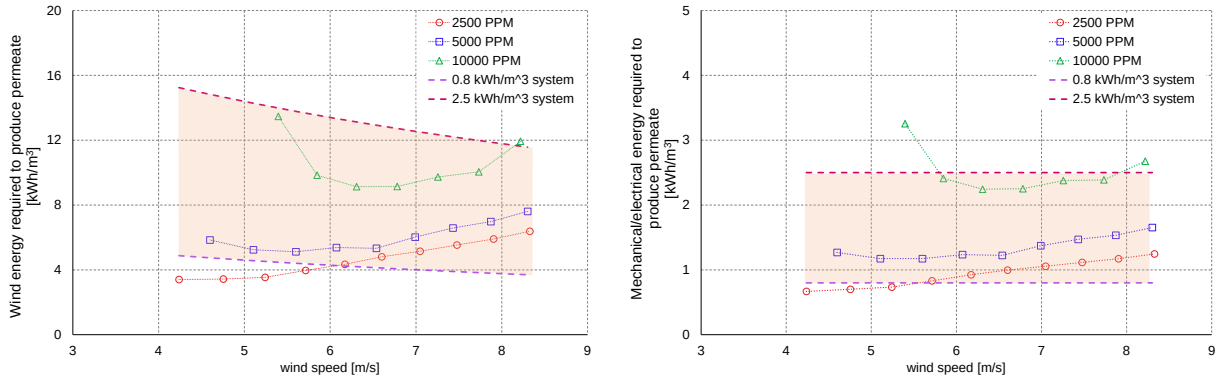

Figure 13: Energy required to produce one cubic meter as a function of wind speed: left – wind energy; right – mechanical energy. Data points – present system; shaded area – conventional BW desalination plant.

3.4 Comparison to Existing Systems

This section discusses and compares the D-WPD system with published wind-powered desalination systems. A summary is shown in Table 1. As previously mentioned, wind-powered desalination systems are divided into three main categories: (i) desalination plants using wind-turbine-generated electricity that is coupled to the grid [26–29]; (ii) stand-alone desalination plants powered by electricity generated directly from wind turbines [20,22,24,25,63–65]; and (iii) stand-alone desalination plants with direct mechanical integration to a wind turbine [33–35,66].

Grid-coupled desalination plants typically operate at medium (~30kW) to large (up to ~2.5 MW) scales and beyond, providing water for regional use [26–29]. On low-wind days, the plant may reduce its permeate production rate, but is typically able to use other energy sources, as storage or grid power to run the desalination process and stabilize the permeate production. These systems operate similarly to conventional grid power-based desalination plants, with high-end controllers and sensors, ERD [62], and optimized operation of the desalination process. This usually yields high overall efficiencies, thus producing low SEC.

In contrast, stand-alone systems experience large variability in the available power due to the fluctuating nature of the wind. Thus, the system design and feed water TDS determine the permeate production, rejection, recovery and other system parameters for each wind speed.

In this manner, stand-alone direct electrically-based systems possess a considerable advantage over direct mechanically-based systems due to their ability to vary pump power and system load. Thus, control the system pressure/flow rate, with only a moderate influence from the wind variability. This advantage multiplies when an electrical storage system is coupled to

the system, enabling an almost constant production of permeate flow rate and quality. However, a study by Carte et al. [67] demonstrated, using simulations, that a large direct electrical-based coupling is not feasible at highly fluctuating wind conditions. Additionally, these systems suffer from efficiency losses in the generators, inverters, transformers and motors [16–18,22,64], whereas smaller systems typically suffer from higher relative losses. In addition, a direct electrical coupling between a generator and a pump motor can create electrical harmonics when a system experiences rapid load or wind speed changes [25]. This may require energy storage or flywheels to smoothen the electrical surges, thereby increasing the system's cost. On the other hand, electricity generation can be used to directly remove ions from the water by coupling the generator directly to an electrodialysis (ED) system. This can achieve high recovery rates and relatively smooth operation at fluctuating wind conditions [64].

In contrast, direct mechanical integration between a turbine and a desalination system eliminates the need for power electronics. This simplification results in a more reliable and cost-effective system. In addition, eliminating power electronics reduces the overall carbon footprint of the system while supporting a more efficient energy transfer process to produce fresh water. However, direct mechanical systems are exceptionally susceptible to wind fluctuations, as the wind speed impacts both the pump speed and available torque. Therefore, without a system controller, both the permeate flow rate and rejection rate are sensitive to these fluctuations, as demonstrated in the previous section. Consequently, these systems often necessitate water storage. As previously mentioned, larger systems tend to have lower relative losses, increasing the overall system efficiency, SEC and relative permeate cost. However, since these systems were only studied at small scales for off-grid applications ($A < 30\ \mathrm{m}^2$), future studies should investigate the economical and mechanical feasibility of larger systems in addition to the influence of long-term wind fluctuation on the desalination module and its reliability.

The system was compared to several studies investigating stand-alone wind-powered desalination plants, either by electricity generated directly from wind turbines [20,22,24,25,63–65], or by a direct mechanical integration to a wind turbine [33–35,66]. Different system parameters (see Table 1) were compared at wind speeds of 4-8 m/s, representing both the typical wind speed range at low heights, corresponding to small-scale systems, and the average studied wind speeds. For each system, based on the available parameters presented in their study, we compare the daily and relative desalination capacity, system size, operation pressures, system maximum and average hydraulic efficiencies $\eta_{\mathrm{sys,max}}$ and $\eta_{\mathrm{sys,avg}}$ (defined in eqn. (4)), rejection, recovery and specific energy consumption ($\mathrm{SEC}_{\mathrm{mech}}$ and $\mathrm{SEC}_{\mathrm{wind}}$, defined in (22) and (23)). To

calculate SEC_{wind} for studies that presented only SEC_{mech}, or vice versa, we assumed an average power coefficient of $30\% < C_P < 35\%$. This is a relatively high average power coefficient for small to medium size wind turbines operating at wind speeds of 4-8 m/s, thus producing a conservative comparison to our system. All systems studied, except [33], have an electronic control system to regulate the pump speed, module pressure, or electricity production and storage. Though, part of the controllers used not only did not improve the system performance, but instead, seemed to reduce the system efficiency and permeate production [33–35].

Despite not having a system controller and its small size, the D-WPD outperforms the direct mechanical [34,35] and electrical [64] wind power BW desalination systems in specific energy consumption, relative efficiency, and relative desalination capacity. However, similar system efficiency and relative desalination capacity were achieved by Park et al. [63], although with higher SEC by utilizing electricity generation and storage. Conversely, from the obtained data [63], at low wind speeds, the turbine power coefficient appears to surpass the Betz limit, implying that wind turbine blockage corrections were not considered. Thus we can assume that the D-WPD system further outperforms [63]. Similarly, higher turbine power output than the stated rated power was obtained from data presented in [65].

The two main reasons the D-WPD maintains low SEC are: (1) relatively high system efficiency; and (2) relatively high recovery rate. Compared to the published wind-powered desalination systems, the system's relatively high recovery rate is a combination of the utilization of a module with high performance at high pressures and a relatively low feed flow rate to module surface area. The high system efficiency is achieved by correctly matching the required desalination power and available wind power, in addition to using a relatively high-efficiency wind turbine $15\% < C_P < 25\%$, an efficient membrane-based pump leading to relatively high pumping efficiencies in the range $50\% < \eta_{pump} \equiv \dot{W}_{hyd} / \dot{W}_{shaft} < 70\%$. Additionally, by adjusting the system to match a specific salinity range, even lower specific energy consumption is achievable.

Compared to the other proposed systems, the main disadvantage of the D-WPD system is the lack of permeate flow rate control. Thus, an elevated storage tank can be integrated to regulate the permeate flow rate. A storage tank can also maintain the module decontamination by backwashing it when wind speeds are below the turbine cut-in speed. A commercial D-WPD system will also require a system break at high wind speeds. This can be achieved using an overpressure safety valve to increase the load on the system.

In addition to wind energy, the energy for a desalination process can be compared to other means of renewable energy such as hydro, solar, and wave. However, hydro energy-based desalination systems are more similar in their operation to conventional desalination systems producing electricity to drive the desalination process. Similarly, wave power-based desalination systems are generally focused on SW desalination, generally considered high cost and unsuitable as small-scale off-grid systems [68,69]. Nevertheless, solar energy-based desalination systems can compete with small-scale, wind-powered systems [70]. The specific electrical power consumption, SEC_{elec}, of an efficient small-scale PV-RO system to desalinate brackish water, $2{,}000\ \text{PPM} < c_f < 5{,}500\ \text{PPM}$, is 2 kWh/m^3, and can reach as low as SEC_{elec} = 1.1 kWh/m^3 [61,71,72]. Additionally, PV electrical power production is cheaper than wind-based. In contrast, the D-WPD system requires a smaller land use, and does not require any electrical components which has the protentional to yield a more economical permeate production than small-scale PV systems. Accordingly, an economic comparison should be performed in regions with high solar and wind density.

With low specific energy consumption, low system complexity compared to previous studies, and a high relative desalination capacity, the D-WPD offers a low-cost solution for off-grid wind-powered small-scale desalination. Due to the turbine's low noise emission and the reduced probability of bird strikes, the D-WPD is ideal for operating near small communities.

Table 1: Summary of D-WPD system to previous wind-powered desalination studies

Paper	Year	Study Type	TDS [mg/l]	Wind-Desalination System Type	Controller	Desalination Capacity at 8 m/s [m^3/day]	Wind Turbine Size [m^2]	Relative desalination capacity at 8 m/s [m^3/m^2day]	Operation Pressure	Evaluated Wind Speeds [m/s]	Max System Efficiency	Average System Efficiency	Salt Rejection	Average Recovery at 4-8 m/s	$SEC_{elec/mech}$ at 4-8 m/s [kWh/m^3]	SEC_{wind} at 4-8 m/s [kWh/m^3]
D-WPD	2023	experiment	2500	direct - MC	no	0.75	0.8	0.94	3-25	4-8	17.50%	12.40%	97.5%	65%	0.7-1.2	3.4-6
			5000			0.62		0.78				13.40%	96.5%	55%	1.2-1.6	5.1-7.1
			10000			0.4		0.50				14.20%	95%	45%	2.2-3.3	9.1-13.5
D-WPD (medium size)	2023	simulation	2500	direct - MC	no	>20	16	>1.2	3-40	2-10	≈26	≈20%	90%-97%	>0.6	< 1	<4
			5000			>15		>1						>0.6	≈1	<4
			10000			>12		>0.75						>0.5	< 2	<8
[34]	1992	experiment	2000	direct - MC	Yes	0.52	12.6	0.04	6-11	2-8	≈9.5%	6%	82.40%	9.7%	≈6-72	≈30-180
			4000			0.45		0.04					85.90%	9.1%		≈38-205
			6000			0.38		0.03					81%	9.3%		≈45-240
[35]	2002	experiment	2700	direct - MC	Yes	≈3	14.5	0.21	5.2-7.2	3.5-9	≈13%	≈7%	96.8%-97.8%	23%	≈2.1-8	≈7-28
			3500			≈4		0.28				≈9%		19%		
[63]	2011	simulations	2750	direct - EC	Yes	≈2.5	2.5	0.98	~10	3.7-8.7	≈16%	≈10%	83%-92%	15%-40%	1.6-2.8	≈5-10
			5500			1.8		0.71					65%-91%	3%-25%	2.8-17	≈9-50
[64]	2016	experiment	5000	direct - EC	Yes	≈0.72	≈1.55	0.48	-	2-10	≈9%	≈4.5%	92%	85%-94%	3.2-4.4	≈10-15
[33]	2009	experiment	35000*	direct - EC	No	N/A	19.6	N/A	N/A	5-12	≈<1%	≈<1%	N/A	≈15%	N/A	N/A
[66]	2003	calculations	35000*	direct - EC	Yes	2410	≈3000	0.80	N/A	8	N/A	≈40%	N/A	N/A	4-8	≈10-20
[65]	2004	partial experiment	35000	direct - EC	Yes	0.7776	7.1	0.11	34-55	7-9	N/A	N/A	97-99	2.5%-12.5%	N/A	N/A
[20]	2002	simulation	40000	direct - EC	Yes	8.5	≈15	0.57	40-60	5-15	N/A	N/A	99%	N/A	3.2-4.5	≈10-15
[29]	2005	experiment	35500	Not-direct	Yes	19	≈40	0.48	55.00	4.5-13	N/A	N/A	99%	37%	7	≈18-30
[25]	2004	experiment	36000	direct - EC, storage and ERD	Yes	N/A	N/A	N/A	65	N/A	N/A	N/A	98.60%	30%	7.5	≈21
[22]	1997	simulations	N/A	direct - EC, storage	Yes	5	19.6	0.25	40-60	4-8	N/A	N/A	N/A	N/A	25-33	80-100
[24]	2018	simulation	33000-38000	direct - EC, w/wo storage	Yes	3-20	78.5	0.25	33-53	N/A	N/A	N/A	98.3%-99.5%	13%-14%	9-16	≈30-45

4 Conclusions

In this paper, a novel direct wind-powered desalination (D-WPD) system was experimentally studied for brackish water desalination. A small-scale vertical axis wind turbine, mounted in a wind tunnel, was mechanically interfaced to a positive displacement, high-pressure pump and operated without electricity production or a system controller. The pump was coupled to an RO-based desalination system and used to drive brackish water with TDS levels of 2,500 ppm to 10,000 ppm through the RO module.

An extensive parametric study of the system was performed. Accordingly, the influence of the feed water salinity, module loading, and wind speed on the system's performance and additional system parameters was studied. The empirical and theoretical relationship between the various parameters were developed and explained. Furthermore, the parametric study demonstrated the capability to achieve high efficiency under a variety of design configurations.

To determine the system's performance under typical field conditions, measurements were made for commonly-encountered wind speeds, namely 4 m/s to 8.5m/s, under a constant valve setting. The study showed that, despite its small scale, $A = 0.8\ \mathrm{m}^2$, the D-WPD system can produce a daily permeate yield of up to $Q_{\mathrm{per}} \approx 0.6\ \mathrm{m}^3/\mathrm{day}$ at $\overline{U_\infty} = 6\ \mathrm{m/s}$. Moreover, the stand-alone system demonstrated operation at a virtually constant average efficiency of $\bar{\eta}_{\mathrm{sys}} \approx 13.5\%$, for a wide range of wind speeds and salinities. This results in a practical and inexpensive wind-based desalination system, operating with low specific wind energy consumption of $\mathrm{SEC}_{\mathrm{wind}} = 3.4\text{-}8\ \mathrm{kWh/m}^3$ for feed water at TDS levels up to 5,000 ppm, corresponding to $\mathrm{SEC}_{\mathrm{elec}} = 0.7\text{-}1.7\ \mathrm{kWh/m}^3$, and $\overline{\mathrm{SEC}}_{\mathrm{wind}} = 10.7\ \mathrm{kWh/m}^3$ for 10,000 ppm. Moreover, based on previous studies, a considerable increase in efficiency is projected (up to 60%) with system upscaling.

Subsequently, the D-WPD was compared to published wind-powered desalination investigations. Despite its size and the lack of a system controller, the D-WPD surpasses previous studies in specific energy consumption, relative efficiency, and relative desalination capacity. Therefore, the D-WPD potentially provides a low-cost solution for off-grid wind-powered small-scale desalination due to its low SEC, high relative desalination capacity, and low system complexity compared to previous wind-based desalination studies. Additionally, the turbine's low noise emission and the reduced probability of bird strikes make it an ideal choice for off-grid operation. In the quest to obtain a simple and low-cost solution for wind-powered

desalination systems, future studies should investigate the economical and mechanical feasibility of larger direct systems in addition to the influence of long-term wind fluctuation on the desalination system and its reliability.

References

[1] Masson-Delmotte, V., P. Zhai, H.-O. Pörtner, D. Roberts, J. Skea PRS, A. Pirani, W. Moufouma-Okia, C. Péan, R. Pidcock, S. Connors, J.B.R. Matthews, Y. Chen, X. Zhou, M.I. Gomis, E. Lonnoy TM, M. Tignor (eds.)T. Waterfield. IPCC, 2018: global warming of 1.5°C. 2019.

[2] WWAP (United Nations World Water Assessment Programme). The United Nations world water development report 2014: water and energy. Paris, France: 2014.

[3] Caldera U, Breyer C. Assessing the potential for renewable energy powered desalination for the global irrigation sector. Sci Total Environ 2019;694:133598. https://doi.org/10.1016/j.scitotenv.2019.133598.

[4] Isaka M. Water desalination using renewable energy, IEA-ETSAP and IRENA Technology Policy Brief I12. 2013.

[5] International Desalination Association. IDA water security handbook. 2018.

[6] Rothausen SGSA, Conway D. Greenhouse-gas emissions from energy use in the water sector. Nat Clim Chang 2011;1:210–9. https://doi.org/10.1038/nclimate1147.

[7] Tal A. Addressing desalination's carbon footprint: The Israeli experience. Water 2018;10. https://doi.org/10.3390/w10020197.

[8] Lotfy HR, Staš J, Roubík H. Renewable energy powered membrane desalination — review of recent development. Environ Sci Pollut Res 2022;29:46552–68. https://doi.org/10.1007/s11356-022-20480-y.

[9] Kim J, Park K, Yang DR, Hong S. A comprehensive review of energy consumption of seawater reverse osmosis desalination plants. Appl Energy 2019;254. https://doi.org/10.1016/j.apenergy.2019.113652.

[10] Nayar KG, Lienhard V JH. Brackish water desalination for greenhouse agriculture: Comparing the costs of RO, CCRO, EDR, and monovalent-selective EDR. Desalination 2020;475. https://doi.org/10.1016/j.desal.2019.114188.

[11] Menachem E, et al. Membrane distillation at the water-energy nexus: limits, opportunities, and challenges energy. Energy Environ Sci 2018;11:1117–96.

[12] Siddiqi A, Anadon LD. The water-energy nexus in Middle East and North Africa. Energy Policy 2011;39:4529–40. https://doi.org/10.1016/j.enpol.2011.04.023.

[13] World Health Organization. Guidelines for drinking-water quality, 4th edition: 1st addendum 2017:1–631.

[14] El Saliby I, Okour Y, Shon HK, Kandasamy J, Kim IS. Desalination plants in Australia, review and facts. Desalination 2009;247:1–14. https://doi.org/10.1016/j.desal.2008.12.007.

[15] Alkaisi A, Mossad R, Sharifian-Barforoush A. A Review of the Water Desalination Systems Integrated with Renewable Energy. Energy Procedia, vol. 110, Elsevier; 2017, p. 268–74. https://doi.org/10.1016/j.egypro.2017.03.138.

[16] Ackermann T. Wind Power in Power Systems, Second Edition. 2012. https://doi.org/10.1002/9781119941842.

[17] Schallenberg-Rodríguez J, Veza JM, Blanco-Marigorta A. Energy efficiency and desalination in the Canary Islands. Renew Sustain Energy Rev 2014;40:741–8. https://doi.org/10.1016/j.rser.2014.07.213.

[18] Saidur R. A review on electrical motors energy use and energy savings. Renew Sustain Energy Rev 2010;14:877–98. https://doi.org/10.1016/j.rser.2009.10.018.

[19] Feron P. Use of Windpower in Autonomous Reverse Osmosis Seawater Desalination. Wind Eng 1985;9:180–99.

[20] Miranda MS, Infield D. A wind-powered seawater reverse-osmosis system without batteries. Desalination 2003;153:9–16. https://doi.org/10.1016/S0011-9164(02)01088-3.

[21] Habali SM, Saleh IA. Design of stand-alone brackish water desalination wind energy system for Jordan. Sol Energy 1994;52:525–32. https://doi.org/10.1016/0038-092X(94)90660-2.

[22] Infield D. Performance analysis of a small wind powered reverse osmosis plant. Sol Energy 1997;61:415–21. https://doi.org/10.1016/S0038-092X(97)00082-0.

[23] Neris AS, Giannakopoulos GB, Vovos NA. Autonomous wind turbine supplying a reverse osmosis desalination unit. Wind Eng 1995;19:325–46.

[24] Cabrera P, Carta JA, González J, Melián G. Wind-driven SWRO desalination prototype with and without batteries: A performance simulation using machine learning models. Desalination 2018;435:77–96. https://doi.org/10.1016/j.desal.2017.11.044.

[25] Carta JA, González J, Subiela V. The SDAWES project: An ambitious R and D prototype for wind-powered desalination. Desalination 2004;161:33–48. https://doi.org/10.1016/S0011-9164(04)90038-0.

[26] Loutatidou S, Liosis N, Pohl R, Ouarda TBMJ, Arafat HA. Wind-powered desalination for strategic water storage: Techno-economic assessment of concept. Desalination 2017;408:36–51. https://doi.org/10.1016/j.desal.2017.01.002.

[27] García-Rodríguez L, Romero-Ternero V, Gómez-Camacho C. Economic analysis of wind-powered desalination. Desalination 2001;137:259–65. https://doi.org/10.1016/S0011-9164(01)00235-1.

[28] Ma Q, Lu H. Wind energy technologies integrated with desalination systems: Review and state-of-the-art. Desalination 2011;277:274–80. https://doi.org/10.1016/j.desal.2011.04.041.

[29] Micale G, Rizzuti L, Andrea C. Seawater Desalination. Palermo, Italy: Springer Berlin, Heidelberg; 2009. https://doi.org/10.2174/97816080528511060101.

[30] Witte T, Siegfriedsen S, El-Allawy M. WindDeSalter® Technology: Direct use of wind energy for seawater desalination by vapour compression or reverse osmosis. Desalination 2003;156:275–9. https://doi.org/10.1016/S0011-9164(03)00358-8.

[31] Tzen E. Wind-Powered Desalination-Principles, Configurations, Design, and Implementation. Renew. Energy Powered Desalin. Handb. Appl. Thermodyn., Elsevier Inc.; 2018, p. 91–139. https://doi.org/10.1016/B978-0-12-815244-7.00003-9.

[32] Argaw N, Foster R, Ellis A. Renewable Energy for Water Pumping Applications in Rural Villages, NREL Technical report SR-500-30361. 2003.

[33] Heijman SGJ, Rabinovitch E, Bos F, Olthof N, van Dijk JC. Sustainable seawater desalination: Stand-alone small scale windmill and reverse osmosis system. Desalination 2009;248:114–7. https://doi.org/10.1016/j.desal.2008.05.045.

[34] Robinson R, Ho G, Mathew K. Development of a reliable low-cost reverse osmosis desalination unit for remote communities. Desalination 1992;86:9–26. https://doi.org/10.1016/0011-9164(92)80020-A.

[35] Liu CCK, Jae-Woo P, Migita R, Gang Q. Experiments of a prototype wind-driven reverse osmosis desalination system with feedback control. Desalination 2002;150:277–87. https://doi.org/10.1016/S0011-9164(02)00984-0.

[36] Lee KY, Tsao SH, Tzeng CW, Lin HJ. Influence of the vertical wind and wind direction on the power output of a small vertical-axis wind turbine installed on the rooftop of a building. Appl Energy 2018;209:383–91. https://doi.org/10.1016/j.apenergy.2017.08.185.

[37] Ghasemian M, Nejat A. Aero-acoustics prediction of a vertical axis wind turbine using Large Eddy Simulation and acoustic analogy. Energy 2015;88:711–7. https://doi.org/10.1016/j.energy.2015.05.098.

[38] Keisar D, De Troyer T, Greenblatt D. Concept and operation of a wind turbine driven by dynamic stall. AIAA J 2020;58:2370–6. https://doi.org/10.2514/1.J059487.

[39] Thelander CG, Smallwood KS, Rugge L. Bird Risk Behaviors and Fatalities at the Altamont Pass Wind Resource Area. Subcontract Rep NREL/SR-500-33829 2003:92 pp.

[40] Keisar D, Eilan B, Greenblatt D. High Pressure Vertical Axis Wind Pump. J Fluids Eng Trans ASME 2021;143:1–9. https://doi.org/10.1115/1.4049692.

[41] Aslam Bhutta MM, Hayat N, Farooq AU, Ali Z, Jamil SR, Hussain Z. Vertical axis wind turbine - A review of various configurations and design techniques. Renew Sustain Energy Rev 2012;16:1926–39. https://doi.org/10.1016/j.rser.2011.12.004.

[42] Akwa JV, Vielmo HA, Petry AP. A review on the performance of Savonius wind turbines. Renew Sustain Energy Rev 2012;16:3054–64. https://doi.org/10.1016/j.rser.2012.02.056.

[43] Hagen LJ, Sharif M. Darrieus Wind Turbine and Pump Performance for Low-Lift Irrigation Pumping. Manhattan, Kansas: U.S. Department of Agriculture, Report No. DOE/ARS-3707-20741/81/1; 1981.

[44] Dominy RG, Lunt P, Bickerdyke A, Dominy J. Self-starting capability of a Darrieus turbine. Proc Inst Mech Eng Part A J Power Energy 2007;221:111–20. https://doi.org/10.1243/09576509JPE340.

[45] Koss D, Steinbuch M, Shepshelovich M. Development of two-element NLF airfoils for long endurance flight. 35th Aerosp Sci Meet Exhib 1997;c. https://doi.org/10.2514/6.1997-514.

[46] Kinsey T, Dumas G. Impact of channel blockage on the performance of axial and cross-flow hydrokinetic turbines. Renew Energy 2017;103:239–54. https://doi.org/10.1016/j.renene.2016.11.021.

[47] Ghermandi A, Messalem R. The advantages of NF desalination of brackish water for sustainable irrigation: The case of the Arava Valley in Israel. Desalin Water Treat 2009;10:101–7. https://doi.org/10.5004/dwt.2009.824.

[48] Möllerström E, Gipe P, Beurskens J, Ottermo F. A historical review of vertical axis wind turbines rated 100 kW and above. Renew Sustain Energy Rev 2019;105:1–13. https://doi.org/10.1016/j.rser.2018.12.022.

[49] Carmichael BH, NASA. Low Reynolds number airfoil survey. NASA Contract Rep 1982;1.

[50] Lissaman PBS. Low-Reynolds-Number Airfoils. Annu Rev Fluid Mech 1983;15:223–39.

[51] Miller MA, Duvvuri S, Hultmark M. Solidity effects on the performance of vertical-axis wind turbines. Flow 2021;1:1–15. https://doi.org/10.1017/flo.2021.9.

[52] Miller MA, Duvvuri S, Brownstein I, Lee M, Dabiri JO, Hultmark M. Vertical-axis wind turbine experiments at full dynamic similarity. J Fluid Mech 2018;844:707–20. https://doi.org/10.1017/jfm.2018.197.

[53] Dixon SL. Fluid Mechanics of Turbomachinery. 5 ed. 1998.

[54] Wijmans JG, Baker RW. The solution-diffusion model: a review. J Memb Sci 1995;107:1–21. https://doi.org/10.1016/0376-7388(95)00102-I.

[55] Lee J, Kim S. Predicting power density of pressure retarded osmosis (PRO) membranes using a new

characterization method based on a single PRO test. Desalination 2016;389:224–34. https://doi.org/10.1016/j.desal.2016.01.026.

[56] Dražević E, Košutić K, Freger V. Permeability and selectivity of reverse osmosis membranes: Correlation to swelling revisited. Water Res 2014;49:444–52. https://doi.org/10.1016/j.watres.2013.10.029.

[57] Bason S, Kaufman Y, Freger V. Analysis of ion transport in nanofiltration using phenomenological coefficients and structural characteristics. J Phys Chem B 2010;114:3510–7. https://doi.org/10.1021/jp911615n.

[58] Ritt CL, Stassin T, Davenport DM, DuChanois RM, Nulens I, Yang Z, et al. The open membrane database: Synthesis–structure–performance relationships of reverse osmosis membranes. J Memb Sci 2022;641:119927. https://doi.org/10.1016/j.memsci.2021.119927.

[59] Becker N. Water Policy in Israel. Tel Hai: Springer Netherlands; 2013. https://doi.org/10.1007/978-94-007-5911-4.

[60] Pan SY, Haddad AZ, Kumar A, Wang SW. Brackish water desalination using reverse osmosis and capacitive deionization at the water-energy nexus. Water Res 2020;183:116064. https://doi.org/10.1016/j.watres.2020.116064.

[61] Li S, Cai YH, Schäfer AI, Richards BS. Renewable energy powered membrane technology: A review of the reliability of photovoltaic-powered membrane system components for brackish water desalination. Appl Energy 2019;253:113524. https://doi.org/10.1016/j.apenergy.2019.113524.

[62] Al-Karaghouli A, Kazmerski LL. Energy consumption and water production cost of conventional and renewable-energy-powered desalination processes. Renew Sustain Energy Rev 2013;24:343–56. https://doi.org/10.1016/j.rser.2012.12.064.

[63] Park GL, Schäfer AI, Richards BS. Renewable energy powered membrane technology: The effect of wind speed fluctuations on the performance of a wind-powered membrane system for brackish water desalination. J Memb Sci 2011;370:34–44. https://doi.org/10.1016/j.memsci.2010.12.003.

[64] Malek P, Ortiz JM, Schulte-Herbrüggen HMA. Decentralized desalination of brackish water using an electrodialysis system directly powered by wind energy. Desalination 2016;377:54–64. https://doi.org/10.1016/j.desal.2015.08.023.

[65] Moreno F, Pinilla A. Preliminary experimental study of a small reverse osmosis wind-powered desalination plant. Desalination 2005;171:257–65. https://doi.org/10.1016/j.desal.2004.06.191.

[66] Witte T, Siegfriedsen S, El-Allawy M. WindDeSalter® Technology: Direct use of wind energy for seawater desalination by vapour compression or reverse osmosis. Desalination 2003;156:275–9. https://doi.org/10.1016/S0011-9164(03)00358-8.

[67] Carta JA, González J, Cabrera P, Subiela VJ. Preliminary experimental analysis of a small-scale prototype SWRO desalination plant, designed for continuous adjustment of its energy consumption to the widely varying power generated by a stand-alone wind turbine. Appl Energy 2015;137:222–39. https://doi.org/10.1016/j.apenergy.2014.09.093.

[68] Leijon J, Boström C. Freshwater production from the motion of ocean waves – A review. Desalination 2018;435:161–71. https://doi.org/10.1016/j.desal.2017.10.049.

[69] Davies PA. Wave-powered desalination: Resource assessment and review of technology. Desalination 2005;186:97–109. https://doi.org/10.1016/j.desal.2005.03.093.

[70] Abdelkareem MA, El Haj Assad M, Sayed ET, Soudan B. Recent progress in the use of renewable energy sources to power water desalination plants. Desalination 2018;435:97–113. https://doi.org/10.1016/j.desal.2017.11.018.

[71] Alghoul MA, Poovanaesvaran P, Mohammed MH, Fadhil AM, Muftah AF, Alkilani MM, et al. Design and experimental performance of brackish water reverse osmosis desalination unit powered by 2 kW photovoltaic system. Renew Energy 2016;93:101–14. https://doi.org/10.1016/j.renene.2016.02.015.

[72] Schäfer AI, Broeckmann A, Richards BS. Renewable energy powered membrane technology. 1. Development and characterization of a photovoltaic hybrid membrane system. Environ Sci Technol 2007;41:998–1003. https://doi.org/10.1021/es061166o.